CONSTRAINING THE PROPERTIES OF KNE BASED ON ZWICKY TRANSIENT FACILITY SEARCHES FOR 13 NEUTRON STAR MERGERS

Priyadarshini Rajkumar[1] Shreya Anand [2]
September 25, 2020

ABSTRACT

In their third observing run (O3), LIGO and Virgo detected gravitational-wave (GW) candidates from several neutron star-black hole (NSBH) and binary neutron star (BNS) mergers. The Zwicky Transient Facility (ZTF), an optical time-domain survey telescope, followed-up thirteen of these GW events in search of Kilonovae (KNe; electromagnetic counterparts to GW events). However, no KNe were found. To assess the implications on potential KN emission based on the upper limits, empirical limits on the KN peak magnitude and evolution rate were determined. One shortcoming of these analyses was the assumption that all peak magnitudes and evolution rates are equally likely. In this work, we present a method to improve upon this assumption by comparing to light curves generated using radiative-transport based KN models, parameterized by ejecta mass and inclination angle. Specifically, we construct priors informed by these KN models to identify regions of parameter space where particular luminosities and evolution rates are improbable. We factor color evolution into the decay rates, important as observations of GW170817 have shown that photometric behavior of a KN differs in different bands. Using our band-specific priors, more realistic constraints are placed on KN source properties. Finally, we close with an application of this methodology to derive constraints on KN ejecta masses.

1. INTRODUCTION

1.1. What are gravitational-Waves? What are its sources?

Gravitational waves (GWs) are perturbations in space-time which have opened a new window for astronomers to obtain insights on some of the universe's most dynamic events. Since GWs are very weak (strain $\sim 10^{-21}$), sensitive interferometers and complex statistical techniques are required to detect them. Commonly, templates of predicted waveforms (from general relativity) for various types of astrophysical events are matched against the observed data stream to detect GW signals.

To the lowest order, gravitational radiation is a quadrupolar phenomenon. This is because the monopole, electric, and magnetic dipole gravitational radiation are prohibited due to the conservation of energy, translational, and angular momentum, respectively (Riles 2013). Since GW perturbations are minuscule, ground-based GW detectors such as the LIGO and Virgo can only detect a specified range of frequencies of GWs. Examples of systems that change their quadrupole moment and emit measurable GWs include merging Black holes (BHs) and Neutron Stars (NS), supernova explosions, and rotating neutron stars with deformed crusts. Thus far, all the GW signals detected by LIGO were emitted by compact binary mergers (Miller 2017).

1.2. Detection of GW events

On September 14, 2015, LIGO reported the first direct direction of a GW signal (referred to as GW150914) from the coalescence of binary black holes (BH-BH) (Abbott et al. 2016). GW150914 and subsequent detections of GW signals from other BH-BH mergers during the first observation run (O1) gave an empirical way to test theories of gravity, space, and time. (Abbott et al. 2019) However, even with the addition of another GW detector (Advanced Virgo) and sensitivity upgrades, the GW signals have relatively poor sky localization (generally more than 1000 square degrees). Although important source properties (e.g. chirp mass) can be extracted from GWs, without the precise sky localization, details such as the host galaxy, the specific environment in which the merger took place cannot be known. Such information is vital for answering a range of fundamental questions in physics and astrophysics.

[1] Department of Physics and Astronomy, Texas Tech University, Box 1051, Lubbock, TX 79409-1051, USA; e-mail: priyadarshini.rajkumar@ttu.edu

[2] Division of Physics, Mathematics, and Astronomy, California Institute of Technology, 1200 E California Blvd, Pasadena, CA 91125, USA; e-mail: sanand@caltech.edu

1.3. *Electromagnetic (EM) counterparts to GW events*

In addition to emitting GW radiation, the merger of a NS with another NS or with a BH are potential sources of electromagnetic (EM) radiation (Nakar 2019). Several theoretical and observational studies have associated BNS and BH-NS mergers with short gamma-ray bursts (sGRB) (Fong et al. 2013). The tightly collimated GRB and its afterglow in X-ray, optical and radio bands can be easily detected only if the beam points towards the Earth (Nousek et al. 2006). On the other hand, if the GRB is off-axis, its afterglow is significantly weaker at the peak, and the peak time is delayed possibly by days since the sGRB (van Eerten & MacFadyen 2011).

Moreover, during the merger, significant amounts of NS matter are ejected at sub relativistic speeds due to either tidal or hydrodynamical forces. The radioactive decay of r-process elements synthesised in the neutron-rich merger ejecta powers a thermal ultraviolet, optical and near infrared transient, often referred to as a kilonova (KN) (Li & Paczyński 1998). Unlike the sGRB afterglow emission, a KN is more isotropic and is one of the best targets for EM counterpart follow-up observations (Metzger 2019). Though BBH mergers are great sources of GW radiation, they not expected to generate EM radiation as no matter is accreted or ejected during tidal disruption at merger.

1.4. *Past joint EM and GW observations*

1.4.1. *GW170817*

The reward of simultaneous detection of EM and GW radiation was realized on August 17, 2017 when the LIGO-Virgo detectors reported the first direct detection of GWs, now termed as GW170817, from a BNS merger (Abbott et al. 2017). Though GW170817 was initially a single detector event, other detectors in operation soon recorded the GW chirp, reducing its localization area down to 30 sq.degrees. Within seconds after the end of GW chirp, a short flash of gamma rays were independently recorded by the Fermi Gamma-ray Burst Monitor and by the INTEGRAL gamma-ray observatory (Goldstein et al. 2017). Subsequently, EM radiation from GW170817 was detected across the whole spectrum (see Cowperthwaite et al. 2017, for example).

Several disparate branches of physics and astrophysics were impacted by this joint EM and GW detection. It provided smoking gun evidence that binary neutron star mergers were capable of synthesizing the heaviest r-process elements (Kasliwal et al. 2019). It also offered a unique opportunity to obtain a measurement of the Hubble constant (see Hotokezaka et al. 2018, for example) and to constrain the equation-of-state (EOS) of dense nuclear matter (see Radice et al. 2018, for example). Additionally, late-time observations (Mooley et al. 2018) showed that GW170817 was accompanied by a successful-jet cocoon.

1.4.2. *EM observations during O3*

LIGO's third observing run (O3), which lasted 11 months, yielded several tens of merger candidates. While the majority were binary black hole candidates, there were a total of 15 neutron star-black hole and binary neutron star candidates identified. Several teams, including Global Relay of Observatories Watching Transients Happen (GROWTH; (Kasliwal et al. 2020)), Electromagnetic counterparts of gravitational wave sources at the Very Large Telescope (ENGRAVE; Levan 2020), Global Rapid Advanced Network Devoted to the Multi-messenger Addicts (GRANDMA; (Antier et al. 2020)), GOTO (Gompertz et al. 2020), All Sky Automated Survey for SuperNovae (ASAS-SN; (Shappee et al. 2014)), Asteroid Terrestrial Last Alert System (ATLAS; Tonry et al. 2018), Panoramic Survey Telescope and Rapid Response System (Pan-STARRS; (Chambers et al. 2016)), MASTER-Net (Lipunov et al. 2017) and Dark Energy Survey Gravitational Wave Collaboration (DES-GW; Soares-Santos et al. 2017) conducted wide-field searches within the skymaps of BNS and NSBH candidates and pursued follow-up of interesting transient candidates found therein, but no plausible EM counterparts were found (Coughlin et al. 2019b).

1.4.3. *What are the challenges?*

Unlike other transients, EM counterparts to GW events are rapidly evolving light curves, which fade and redden in just a few days (Nakar 2019), hence, a rapid follow-up is vital to realize the full scientific potential of joint EM/GW detections. There are however significant challenges for the joint EM/GW endeavour. Factors like large positional uncertainty of GW sources, progenitor visibility on the sky, long integration times to reach the required depth, and a large number of false positives (such as unrelated SNe, asteroids) in probability contour maps make it challenging to quickly localize the EM counterparts to GW events. With more GW detectors expected to be operational and sensitivity upgrades, we strongly expect an increased detection rate of GW signal of EM bright events over the next few years. Although the multi-messenger discovery of GW170817 clarified some of the decades-old mysteries, we need many more such discoveries and follow-ups to answer other questions it left us with. The questions include (i) What insights

we gain about the properties of BNS and NSBH mergers from detections and non-detections? (ii) what do our observations from 03 imply about our BNS vs. NSBH detection prospects?

1.5. *EM and GW searches with the Zwicky Transient Facility*

1.5.1. *Existing strategies for EM Follow-up*

The GW sky localization regions can span 100-1000 square degrees demanding effective strategies to optimize the follow-up efforts. The two common options are galaxy-targeted and synoptic survey strategy. The synoptic survey strategy is commonly employed by follow up facilities with large apertures and imagers with large fields of view (FOV) such as the Zwicky Transient Facility (ZTF). The idea here is to strategically search the entire probability region for new transients with tiles of the size of the telescope's field of view. The four currently available methods for skymap tiling are MOC, ranked, hierarchical and greedy. Efficiencies of these algorithms are analysed in (Coughlin et al. 2018). On the other hand, telescopes with small FOVs (spanning a few sq. arcmin to a few sq. deg), use the galaxy-targeted strategy, which is built on the model that the merger is more likely to occur in close proximity to galaxies (Singer et al. 2014). Instead of covering the entire error region, the idea is to observe previously catalogued galaxies (prioritized based on various criteria, such as stellar mass, star formation rate) in the GW sensitivity volume. Since sky area coverage of galaxies is ≈1% within the GW error volumes (Cook et al. 2019), this approach can significantly reduce the sky area searched and the number of false positives.

1.5.2. *EM searches with Zwicky Transient Facility*

ZTF is an optical time-domain survey that is now in operation. The ZTF observing system consists of a CCD camera with 47 square degrees field of view installed on the 48-inch Samuel Oschin Schmidt Telescope at the Palomar Observatory. Despite its large focal plane, ZTF's camera maintains high image quality. With a 30 second exposure, ZTF survey images have a depth of 20.4 magnitudes. In addition to its depth and areal survey speed, ZTF is equipped with fast readout electronics which enables it to scan the sky at a the rapid rate of about 3750 square degrees per hour. Further, ZTF has a complement of three custom filters ZTF-g, ZTF-r, ZTF-i (for a comprehensive review on ZTF instruments and software see Bellm et al. 2018; Masci et al. 2018). ZTF conducts general-purpose public surveys nightly. The public surveys cover the observable Northern sky at a

three-day cadence and the visible Galactic plane every night in g and r bands (Graham et al. 2019).

In addition to the nightly ZTF survey operations, during O3 ZTF conducted Target-of-Opportunity observations within the skymap of each accessible GW trigger. ZTF uses the GROWTH ToO marshal (Coughlin et al. 2019a, Kasliwal et al. 2020), a database designed to automatically ingest Gamma-ray Coordinates Network (GCN) circulars of GWs, GRBs, and neutrino localization, create a galaxy-targeted or synoptic strategy for observations, trigger the telescope queue, and retrieve summary statistics. This framework uses `gwemopt`, an open-source code base for scheduling synoptic and galaxy-targeted observations. Our Target-of-Opportunity (ToO) observations consist of anywhere between 180-300 s exposures depending on the size of the GW skymap. These ToO observations interrupt the nominal survey operations to observe the region dictated by the submitted schedule. Weather plays a large factor in the achieved depth; the maximum depth achievable with 300s exposures is $m_{AB} \approx 22$ on a clear night, but weather has in the past limited the median depth to $m_{AB} \approx 20.5$, even with 300s exposures.
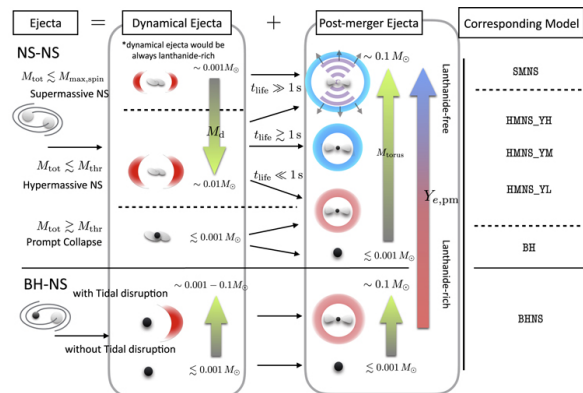
1.6. *BNS vs NSBH*

Fig. 1.— Schematic picture for demonstrating the dependence of the properties of BNS and NSBH ejecta on remnant identity. From (Kawaguchi et al. 2020)

1.6.1. *Ejection process of BNS mergers*

Several different physical processes lead merging BNSs to eject considerable amounts of mass at sub-relativistic velocities. A variety of numerical simulations are done to predict the properties of the ejected material and its observational signatures (Bulla 2019). Using the results, the BNS mass ejection mechanisms are classified into two broad classes .i.e dynamical ejecta and post-merger or secular ejecta. The mass ejection occurring within ∼10 ms during the final stages of the inspiral is referred to as

the dynamical ejecta. This is due to the tidal forces and the shocks that form during the collision of the two NS cores. The bound NS material, having adequate angular momentum, forms an accretion disk surrounding the remnant of the merger within a few orbits. The outflow following this is termed as the secular ejecta. This ejecta mass is launched from the remnant and its torus due to magnetically-driven, disk and neutrino winds. Both of the mass ejection processes and thus the observed signals are strongly impacted by the remnant identity (see Fig. 1). The four ultimate outcomes of a BNS merger are: 1) a BH, 2) a "hypermassive" NS, supported by differential rotation, that collapses to a black hole in less than a second 3) a "supramassive" neutron star, supported by its rigid rotation, that collapses to a black hole on much larger timescales 4) a stable NS (Nakar 2019).

1.6.2. *Ejection process of BH-NS mergers*

The ejection mechanisms of BH-NS mergers are different from those for BNS mergers (see Figure 1). As the orbit decays, the neutron star's gravity becomes equal to the BH's tidal forces. At this distance, called the tidal radius, the NS is totally disrupted by the tidal forces of BH. The properties of the ejecta mass of these systems depend on whether or not the tidal radius is within the innermost stable circular orbit (ISCO) of the BH. If the tidal radius is within ISCO, there is no significant total ejecta mass and no disk is formed. In the other case, some NS material is ejected; part of the unbound ejecta constitutes the dynamical ejecta. The rest of the bound NS material forms a disk around the central BH within 10s. The secular ejecta process of BH-NS mergers is similar to that of BNS mergers whose remnant is a BH. (Metzger 2019)

1.7. *BNS vs NSBH models*

Some major differences in the observational features of the KN from BNS and NSBH mergers include:

- **Reddened Emission**: Numerous studies predict that KNe from NSBH mergers are generally brighter than those resulting from BNS mergers (Kawaguchi et al. 2020). Kasen et al. 2017 predicts that NSBH KNe are dimmer in optical, but brighter in infrared as no polar ejecta is produced at the merger. Further analyses have shown that NSBH KN are brighter in i- and z-band compared to g- and r- band across the parameter space (Anand et al. 2020).

- **Delayed Peak**: Due to longer diffusion timescales, Kawaguchi 2020 predicts that lanthanide fraction of the post-merger ejecta increases which leads to a delay to the peak for NSBH mergers (Kawaguchi et al. 2020).

- **Slower Evolution rates**: NSBH mergers produce ten times more dynamical ejecta creating a high-density and lanthanide rich environment. Consequently, the matter opacity is high and photons diffuse slower out of the dynamical ejecta. This causes the KNe from NSBH mergers to evolve slower than that from BNS mergers (Kawaguchi et al. 2016).

1.8. *Extrinsic Properties of BNS and NSBH mergers*

Another factor to be taken into account is GW detectors' sensitivities. Both the coalescence of NSBH binary and BNS are within the sensitivity range of the detectors. However, the detectors are more sensitive to GWs emitted by NSBH mergers than that of BNS mergers. Therefore, NSBH mergers tend to be more distant, because they can merge in LIGO's sensitive band. GW signals are localized by triangulation of GW arrival times with an array of interferometers. Therefore, a detection made by just the two North American LIGO facilities have a very large sky error region compared to the one made by all the three detectors currently in operation. So, higher the signal to noise ratio, the detection could be made by more detectors and therefore smaller the GW error region. As expected, NSBH mergers had better signal-to-noise ratio and localization than BNS mergers in 03 (Collaboration et al. 2013). However, their larger distance on average compared to BNS mergers can pose significant challenges for counterpart detection.

The outline for this paper is as follows. In section 2, we briefly discuss the work carried out in (Kasliwal et al. 2020), and state and describe our two main objectives. In section 3, we first present a method to construct priors informed by KN models to identify regions of parameter space where particular luminosities and evolution rates are improbable and then we present a way to contraint the ejecta masses. In section 4, we share our premliniary results of this study and in section 5, we summarize our findings and briefly state how our work could used for other projects.

2. OBJECTIVES

During O3, ZTF followed up 13 GW triggers, including NSBH and BNS mergers. Each trigger yielded several tens of candidates that were systematically vetted out using photometric, spectroscopic, and other criteria. Several photometric and spectroscopic facilities were

used to obtain further data for each of the candidates. The searches did not find any plausible candidates that could be associated with GW triggers (Kasliwal et al. 2020). The non-detection of KNe during the entirety of O3, in stark contrast to the immediate identification of a KN after the first BNS merger detection lends us clues as to the nature of the underlying population of detectable KNe. Several studies (see Anand et al. 2020; Andreoni et al. 2020; Kasliwal et al. 2020) have shown that constraints on the KN emission can be placed even in the case of non-detection of a KN. Below, we detail two objectives that build on previous work to constrain kilonova properties.

2.1. *Goal 1: Absolute Magnitude–Decay Rate Constraints*

In this project, we build upon the work presented in Kasliwal et al. 2020, in which the non-detection of a KN in all searches conducted is interpreted as 1) probability of detecting KNe of a given luminosity and decay rate and 2) constraints on the intrinsic luminosity function of KNe. The main steps of this project is discussed below to point the shortcomings of this study and the possibilities of improving it.
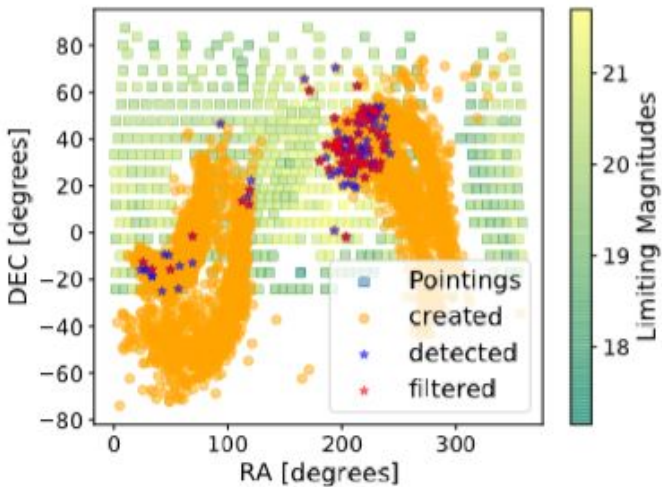

FIG. 2.— The injection and recovery campaign carried out for S200105ae using `simsurvey`. The blocks represent the ZTF pointings and the color scale points to its limiting magnitude. While the orange dots are all the KNe that were injected throughout S200105ae probability region, the purple stars are the detected sources, injected KNe that were observed by ZTF at least once with the necessary depth. The red stars or the filtered sources are those that pass additional criteria such as multiple observations.

Firstly, to assess the implications of the non-detections on potential KN emission, the efficiency (or probability) of detecting a KN of a given magnitude and evolution rate for any given event is determined based on the ZTF upper limits. To accomplish this, an open source

simulator software called `simsurvey`[3](Feindt et al. 2019) is used. The software takes as input the ZTF pointings (the observation time, limiting magnitude, filters, right ascension and declination as defined by field id and ccd id) for the first 3 days of the merger, and the 3D GW skymap for any given GW event. Then, over 10,000 KNe that all peak at a given absolute magnitude and evolve at a same rate are injected throughout the 3D GW probability region (see Fig. 2). Note that this study assumes a empirical model of linear evolution of the KN light curve from its peak absolute magnitude. Based on the ZTF pointings, we classify each of these injected sources as recovered (or detected) if it was observed at least one time by ZTF with the necessary depth. Then the efficiency is computed by dividing the number of recovered KNe by the total number of injected KNe (see Fig.3). For any given GW event followed by ZTF, this
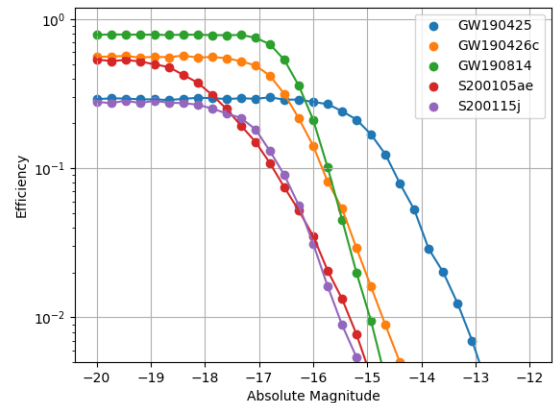

FIG. 3.— Assuming flat photo-metric evolution, we show event-by-event detection efficiency of KN that peak at different absolution magnitudes. We have chosen 5 of 13 GW events followed up ZTF that have low false alarms rates.

process is repeated for various magnitudes (31 luminosity bins between -12 mag to -20 mag) and evolution rates, and a grid of efficiencies is created. A grid of efficiencies for each of the thirteen O3 GW events followed by ZTF is created in the same way.

Since all GW events are independent, we construct a composite efficiency map by convolving the individual grids together (see Fig.4).

Any row of this composite efficiency grid can be converted into constraints on the KN luminosity function using Eq.1, presented in Kasliwal et al. 2020. The KN luminosity function is a simple function that provides

---

[3] https://github.com/ZwickyTransientFacility/simsurvey

guidance on the brightness distribution of KNe.

$$(1 - CL) = \prod_{i=1}^{N} (1 - f_b * p_i) \qquad (1)$$

This formulation assumes that the peak luminosity distribution of KNe is non-uniform, and that some fraction of KNe peak at each given absolute magnitude between [-10, -20]. Then using the above equation (see Eq. 1), for a given confidence level (CL) and evolution rate of the KN, at each absolute magnitude we can solve the maximum fraction of KNe (f_b) brighter than that absolute magnitude, based on `simsurvey` composite detection efficiency p_i for a model with that absolute magnitude and decay rate (see Fig. 5).
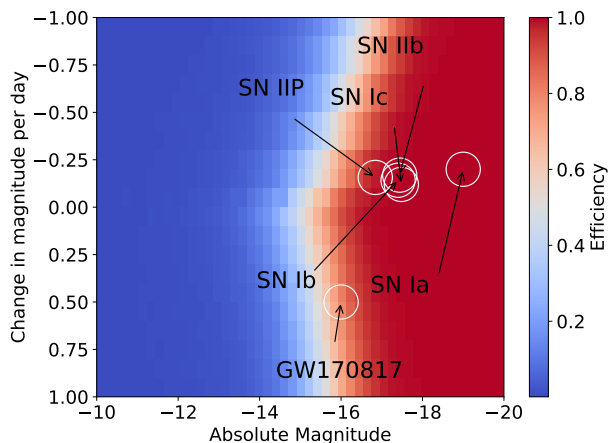
FIG. 4.— The Composite efficiency map constructed using `simsurvey` and based on the ZTF observations in O3. The general observed properties of different types of supernovae and that of the KN of GW170817 are plotted on top of the efficiency map for comparison. Even supernovae, generally expected to be brighter than KNe, do not usually peak at -20 mag. This highlights that there might be areas in the grid where the KNe are improbable.

One shortcoming of these analyses was the assumption that all peak magnitudes and evolution rates are likely. To highlight this, we plot the average observed properties of different types of supernovae in the composite efficiency map (see Fig.4). Generally, supernovae are expected to be brighter than KNe. Even the Type Ia supernova, intrinsically brighter than all other sub-types, does not typically peak at -20. So, it unlikely that a KN, expected to be intrinsically faint, would peak at -20 absolute magnitude. In this paper, we present a way to identify regions of parameter space where particular luminosities and evolution rates are improbable. Specifically, we present how to construct priors (or probability density functions) informed by radiative-transport based KN models, parameterized by ejecta mass and inclination angle. We also show how to use these priors to weight the composite efficiency

map for placing more realistic constraints on the KN luminosity function. In principle, we could directly input KN models parameterized by ejecta mass and inclination angle into `simsurvey` to obtain KN efficiencies for the resulting absmag and decay rate of a given lightcurve. However, we find this to be more computationally expensive and time intensive, as it requires us to repeat our simulations for each new set of models. Further, if any changes to be made to the KN models, grids need to be recreated. In this project we explore a way to directly weight the efficiency grids we already have with priors that relate models to peak magnitudes and decay rate. This not only reduces the parameter space for placing constraints, but also could be quickly and easily be adapted for other models.
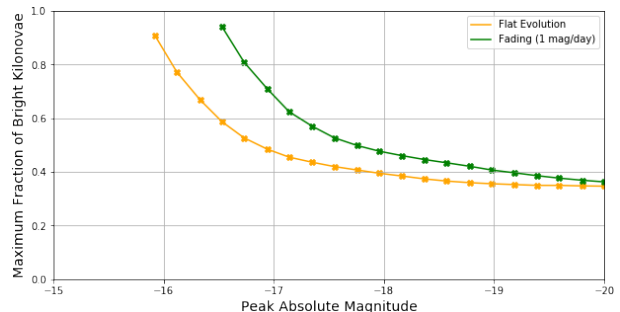

FIG. 5.— Assuming flat photometric evolution (orange dots) and fading by 1 mag day^{-1} (green dots), the constraints on the KN luminosity function are shown at a 90% confidence level. At the bright end, no more than $\approx$ 40% of flat evolving KNe can be brighter than -18 mag. At the faint end, no strong constraints on the luminosity function of KNe could be placed based on ZTF O3 observations. This plot is reproduced from Kasliwal et al. 2020

Another shortcoming of this analysis is the assumption that KNe have the same luminosity in g-,r- and i- bands. However, observations of GW170817 have shown that the photometric behavior of a KN differs in different bands (see Fig. 6; Cowperthwaite et al. 2017). Therefore, color-specific models will yield more accurate results compared to a color-less model employed in Kasliwal et al. 2020. Furthermore, ZTF carried out KN searches in the r-,g-, and i-bands, and some bands were prioritized over the others. So, we factor color evolution into the decay rates and create separate efficiency grids separately for r-,g- and i-bands. Having band-specific efficiency grids also gives us a way to assess the performance of ZTF in terms of filter-sensitive searches.

2.2. *Goal 2: Ejecta Mass Constraints*

Variations in masses, velocities, and compositions of the ejecta, and inclination angle results in different observed KN morphology. Assuming the KN is in the area observed, previous studies (see Andreoni et al.
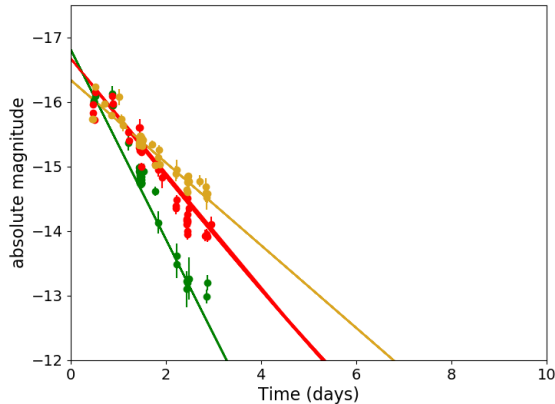
3.1.1. *Model Selection*

We use "surrogate models" (Coughlin et al. 2018) trained on the outputs of the Monte Carlo Radiative-transfer code POSSIS (Bulla 2019). POSSIS is a suite of 2D KN models assuming a two-component ejecta geometry, with an equatorial lanthanide-rich component and a polar lanthanide-poor components. Broadly speaking, the surrogate models, otherwise referred to as phenomenological models, use a machine learning technique to interpolate between data points. For example, this interpolation technique allows us to create a surrogate KN model with ejecta mass of 0.015 $M_\odot$ knowing the KN morphology of models with ejecta mass of 0.01 $M_\odot$ and 0.02 $M_\odot$ in a fixed grid. Both the surrogate models and POSSIS simulate KNe for a combination of four parameters: the inclination or the observer viewing angle (Θ_{obs}), dynamical ejecta mass (M_{dyn}), post-merger or wind ejecta mass (M_{wind}), and half-opening angle for the lanthanide-rich dynamical component.

We assume a 30° half opening angle for both systems and vary the other three parameters. Using the surrogate models, we predict both BNS and NSBH KN light curves for 10 viewing angle from a polar ($\Theta_{obs} = 0°$) to an equatorial ($\Theta_{obs} = 90°$) orientation and for the following ejecta masses: both M_{dyn} and $M_{wind} \in [0.001, 0.1]$ for BNS and both M_{dyn} and $M_{wind} \in [0.01, 0.08]$ for NSBH. So, in total we simulated 810 and 640 KN models for BNS and NSBH, respectively.

FIG. 6.— Brightness as a function of time is plotted for the KN of GW170817 in g-, r-, and i-bands. This plot highlights the difference in the KN evolution in different bands. In the first few days since the merger, this KN peaked brightest in g-band but evolved much faster in the g-band compared to r- and i-bands.

2020; Anand et al. 2020) used median observational upper limits on each night to constrain NSBH KN models at different distances within the GW distance estimate. These model constraints were then converted to constraints on the intrinsic KN properties such as ejecta masses. While using median upper limits to place constraints is an effective way, using injection and recovery of simulated KNe in `simsurvey`, which better quantifies both the degree of variation in the upper limits of individual exposures and the spatial variation of GW distance estimates, would be a more accurate way to place similar constraints. Previously, this methodology using `simsurvey` have been employed to empirically luminosity function of KNe from BNSs and NSBHs. We outline here another application of this methodology to derive constraints on KN ejecta masses.

Constraining the ejecta masses of the KN population could potentially provide us better insights on the amount of r-process material contributed to the formation of KNe, and also relation between binary parameters (EoS, spin, mass ratio) and ejecta mass. This analysis could greatly aid in finding more realistic KN models and could show how even the non-detection of EM allows for stringent constraints on the source parameters.

3. METHODS

3.1. *Goal 1: Constructing Priors*

In this section, we first present a method to construct priors informed by KN models to identify regions of parameter space where particular luminosities and evolution rates are improbable.
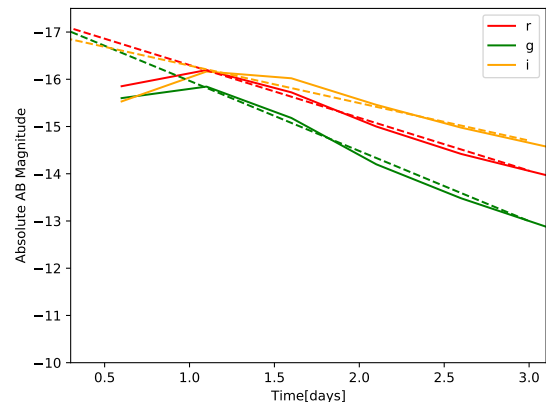

FIG. 7.— A representative of g-, r-, and i-band KNe lightcurves simulated using the surrogate models (parameterized by ejecta masses and inclination angle) for the first three days since the merger. Generally, these lightcurves rise before they begin to decay. This particular KN lightcurve is predicted for $M_{dyn} = 0.005 M_\odot$, $M_{wind} = 0.03 M_\odot$, and $\Theta_{obs} = 30°$. We fit a linear model (dotted line), a reasonable approximation during the first three days, on these lightcurves to extrapolate the peak absolute magnitude and evolution rate.
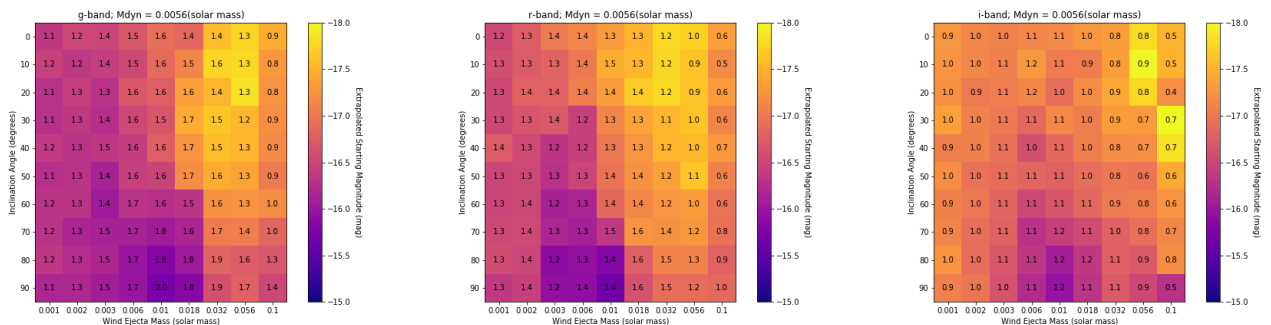
FIG. 8.— KN lightcurves are simulated for a range of viewing angles, dynamical, and wind ejecta masses. Setting the dynamical ejecta mass $M_{dyn} \approx 0.005$, we have mapped the wind ejecta mass and inclination angle to observed KN morphology. Color bar points the trend in peak magnitude and annotations point to the decay rates. The peak absolute magnitude has a strong dependence on the observing angle, with increasingly fainter KNe when moving from a polar ($\Theta_{obs} = 0°$) to an equatorial ($\Theta_{obs} = 90°$) observing angle. Also, higher wind ejecta mass tend to power brighter and slow evolving KNe in g-, r- and i-bands.

3.1.2. Mapping from KN source to observed properties

Having created a large sample of BNS and NSBH KN models, we map from KN source properties (ejecta mass and inclination angle) to observed KN features (peak magnitude and evolution rate). We fit a linear model, a reasonable approximation during the first three days (see Fig.7), to g-, r-, i-band lightcurves of the simulated KNe for combination of source parameters. Since we assume a linear decay of KNe (no rising component as in the simulated KN lightcurves from surrogate models; see Fig.7) in simsurvey injection and recovery campaigns, we choose the vertical intercept of the linear fit as the characteristic peak absolute magnitude of the KN. We repeat this process for all the simulated KN models for both BNS and NSBH case and create grids as such as Fig 8. We notice an expected trend in these grids: Higher ejecta mass and smaller inclination angle models tend to power brighter and more slowly evolving KNe in r-, g- and i-bands during the first three days of the merger.

Gathering the possible values for peak absolute magnitude and decay rate of KNe, we constructed 1D (see Fig.14 and Fig.15) and 2D histograms to determine the distribution of these parameters in different bands. We employ kernel density estimation to alleviate the binning problems with histograms. More specifically, we fit a kernel, in our case a Gaussian curve, on each of data points and then add the kernels to construct a smooth probability density function, which is likely to reflect the true distribution of peak magnitude and decay rate of the simulated KNe. Value at any point of Fig.9 can be interpreted as the relative likelihood of KNe with a given peak absolute magnitude and evolution rate. We refer to these plots (Fig.9) as priors and use these to identify regions of parameter space where particular luminosities and evolution rates of KNe are most probable (trends discussed in Sec.5).

3.2. Goal 2: Constraints on Ejecta Masses

In this section, we outline a novel methodology of using simsurvey to place constrains on the KN source properties such as ejecta masses.

Previously in Kasliwal et al. 2020, Eq.1 represented the constraints on luminosity function of KNe as the maximum fraction of KNe brighter than a given magnitude. Having created priors that directly map the properties of merging binary (ejecta mass and inclination angle) to the properties of the associated KN (peak absmag and decay rate), we could express simsurvey efficiency (or probability of detection) as a function of ejecta mass and inclination angle (earlier it was expressed as a function of peak absmag and decay rate). This allows us to use the same Eq.1 to now represent constraints on KN source properties.

As mentioned earlier, the BNS and NSBH KN models used in this project are parameterized by inclination angle, wind ejecta mass, and dynamical ejecta mass. In principle, we could set any two of these parameters constant and place constraints on the third parameter based on the ZTF observations in O3. To begin with, we fix the inclination angle $\Theta_{obs} = 30°$ and draw constraints on the wind ejecta masses M_{wind} for different dynamical ejecta masses M_{dyn}.

$$(1 - CL) = \prod_{i=1}^{N}(1 - f_m * p_i) \qquad (2)$$

The Eq.2 is interpreted as a function that dictates the maximum allowed fraction f_m of KNe with ejecta mass larger than $xM_\odot$.

Choosing a value for M_{dyn} (say $0.001M_\odot$, we gather the peak absmag and decay rate of the KN lightcurves predicted for a range of M_{wind}. From our event-by-event (weighted or unweighted) efficiency grids, we collect the efficiencies (p_i) for detecting KNe with these
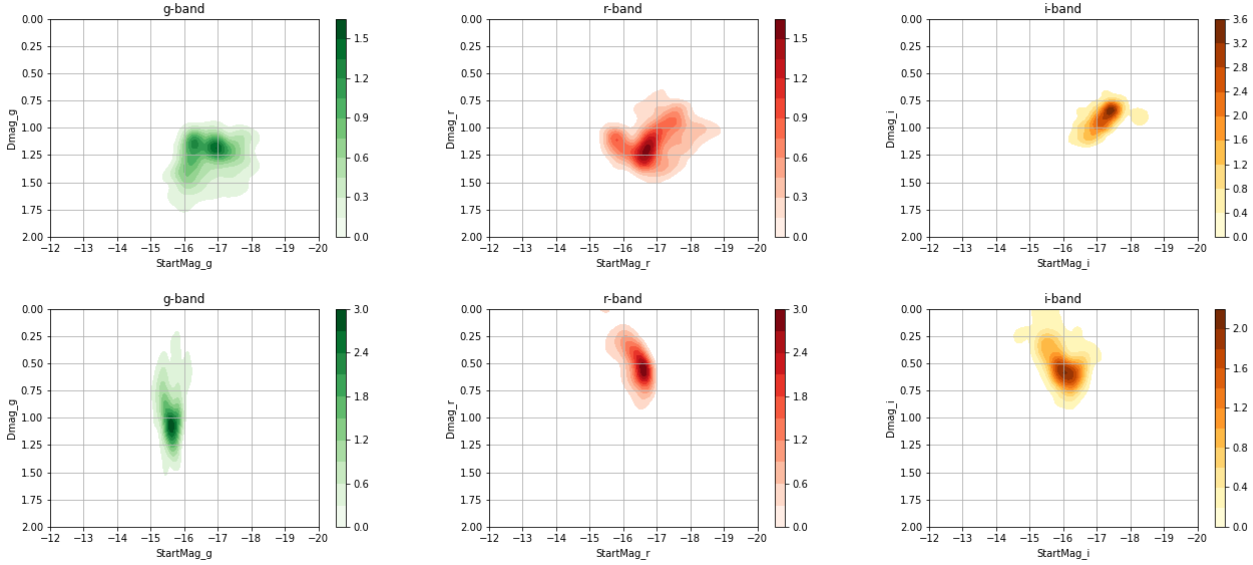
FIG. 9.— Having simulated the KNe for range of merging binary properties such as inclination angle and ejecta masses, we gathered the possible values for KN peak magnitude and evolution rate and created 2D probability distributions for these parameter in different bands. Regions of parameter space where particular luminosities and evolution rates are most probable for BNS KNe are shown on the top and likewise for NSBH KNe at the bottom for g-, r- and i-bands respectively.
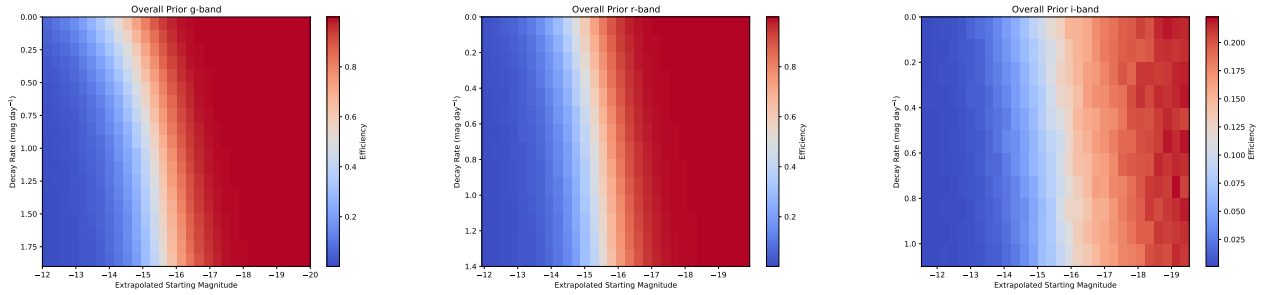

FIG. 10.— Composite efficiency maps created using `simsurvey` and ZTF follow-up observations is shown in g-, r- and i-bands (left to right). The composite efficiency map is created by convolving the efficiency grids of each of 13 GW events followed up ZTF. The color bar in each plot shows the composite recovery efficiency of a KN. The recovery efficiency corresponds to the number of KNe detected by a specific ZTF band divided by the total number of KNe injected according to the 3D GW Skymap. Band-specific efficiency grids provides a visualization of ZTF performance in O3 in different band. Overall, the g- and r- bands have better limiting magnitude than that of i-band.
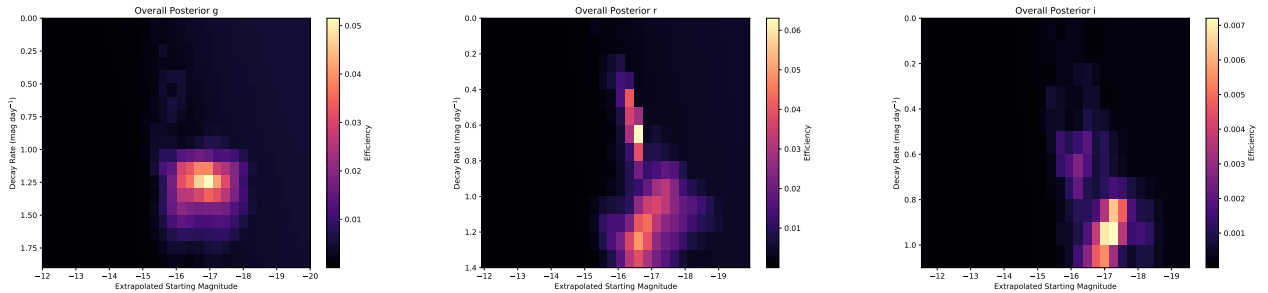

FIG. 11.— The composite band-specific weighted efficiency grids are shown in g-,r-,i-band (left to right). We find that the regions of parameter-space that are least likely for a KN are down weighted and darkened. Consequently, the regions of probable KN peak mag and decay rates are sharply highlighted. It is quickly evident that the ZTF efficiencies at these highlighted regions are considerably low which explains the non-detection of KNe in the entirety O3

gathered observed properties. Then using Eq.2 for a given confidence level (CL), at each reasonable wind ejecta mass we can solve for the maximum fraction of KN having wind ejecta mass larger than that value, based on `simsurvey` detection efficiency.

4. RESULTS

4.1. Goal 1

Following the methodology outlined above, we construct band-specific priors in absmag and evolution rate space for BNS and NSBH mergers (see Fig.9). Using these priors constructed using our choice of KN models(see Sec. 3.1.1), we identify regions of parameter space where particular luminosities and evolution rates are most probable or improbable. Generally, we find that both BNS and NSBH KNe fade faster in g-band compared to the redder (r- and i-bands) bands. Further, we also see an overall trend that NSBH KNe fade slower than BNS KNe. For BNS models, the probability density is highest around the peak absmag of -16.5 mag and the decay rate of 1 mags per day in the redder bands. Likewise for NSBH models, the probability density is highest around -16 peak mag and the decay rate of 0.5 mag in the redder bands.

Secondly, factoring color evolution into decay rates in the KN model used for simsurvey and using ZTF pointings in different bands, we created efficiency grids in separate bands (see Fig.11). From these band-specific efficiency grids, it is quickly evident that ZTF had performed significantly better in g- and r- bands than in i-band for KNe searches in O3. We can attribute this to the small number of i-band observations compared to g- and r-band observations. Further, we notice that in all bands around -16 magnitude the efficiencies drop significantly.

Finally, we weighted the band-specific event-by-event efficiency grids by our priors (Fig. 9) and created an composite weighted efficiency map by convolving the independent event-by-event weighted efficiency grid (Fig.11). We find that the regions of parameter-space that are least likely for a KN are down weighted and darkened in our posterior efficiency grid. Consequently, the regions of probable KN peak mag and decay rates are sharply highlighted. It is quickly evident that the ZTF efficiencies at these highlighted regions are considerably low which explains the non-detection of KNe in the entirety of O3.

4.2. Goal 2

Following are some preliminary results on the constraints of the wind ejecta masses placed following

the methodology presented above.

Since the efficiencies are considerably low in our grids, we use the unweighted efficiency grids in Kasliwal et al. 2020 to draw constraints on the ejecta properties. In the future with more events and better sensitivities, we could easily adapt our code to make use of the weighted efficiencies.
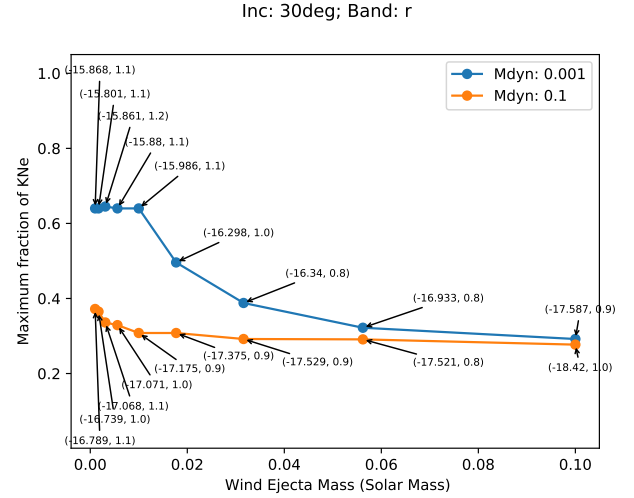

FIG. 12.— For $M_{dyn} = 0.001 M_\odot$ and $0.1 M_\odot$, the constraints on the BNS KN ejecta masses are shown at a 70% confidence level. At the high mass end, no more than $\approx 40\%$ of BNS KNe can have wind ejecta mass higher than $0.05 M_\odot$. At the low mass end, no strong constraints on the BNS KN wind ejecta could be placed based on ZTF 03 observations.
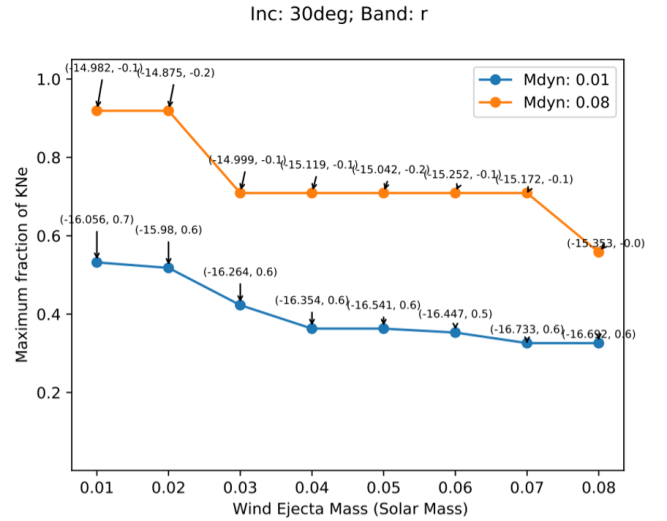

FIG. 13.— For $M_{dyn} = 0.01 M_\odot$ and $0.08 M_\odot$, the constraints on the NSBH KN ejecta masses are shown at a 50% confidence level. For $M_{dyn} = 0.01 M_\odot$, no more than $\approx 40\%$ of NSBH KNe can have wind ejecta mass higher than $0.05 M_\odot$. For $M_{dyn} = 0.01 M_\odot$, no strong constraints could be placed based on ZTF 03 observations since higher dynamical ejecta mass leads to fainter KNe.

For both BNS and NSBH case, increasing the wind ejecta mass leads to both brighter and more slowly

evolving KNe, thus better detection efficiencies. So, we were able to place better constraints at higher wind ejecta masses. However, contrary to the BNS case, we placed poor constraints for higher dynamical ejecta mass for the NSBH case. This is because NSBH dynamical ejecta are lanthanide-rich in composition, i.e. the opacities are high. Consequently, the diffusion timescale for radiation is long. Adding mass to the dynamical ejecta (e.g from 0.01 to 0.08 Msun) thus significantly increases the diffusion timescale and results in dimmer KNe in the first three days of merger.

5. CONCLUSION

We devised a way to weight the grid of efficiencies presented in Kasliwal et al. 2020 by realistic priors which are motivated by KN models. With more events and better sensitivities, the weighted grid of efficiencies could be used to place more realistic constraints on the KN luminosity function. We also investigated into ways of effectively constraining the KN ejecta properties based on the ZTF 03 observations. Generally, we were able to place good constraints for higher dynamical and wind ejecta masses.

Looking ahead, the priors and methodology for weighting our efficiency grids could be useful for more than just to constraint the KN luminosity function. Efforts are being taken by the GROWTH team to use a Bayesian approach to improve the generic KN luminosity function presented in Kasliwal et al. 2020. This approach allows for estimating the posterior probability of a kilonova with a given peak absolute magnitude and decay rate within a GW skymap, assuming that no kilonova was detected. Further, it takes into account the GW event properties that describe the significance of a detected GW signal. Currently, we are working towards a) conducting comparisons between our simsurvey results and the Bayesian results, and b) factoring the astrophysical priors presented in this paper into the bayesian framework, which could place realistic and strong KNe population constraints.

6. ACKNOWLEDGEMENTS

REFERENCES

Abbott, B., Abbott, R., Abbott, T., et al. 2016, Physical Review Letters, 116, doi:10.1103/physrevlett.116.061102

—. 2017, Physical Review Letters, 119, doi:10.1103/physrevlett.119.161101

—. 2019, Physical Review X, 9, doi:10.1103/physrevx.9.031040

Anand, S., Coughlin, M. W., Kasliwal, M. M., et al. 2020, Nature Astronomy, doi:10.1038/s41550-020-1183-3

Andreoni, I., Goldstein, D., et al. 2020, Astrophys. J., 890, 131

Antier, S., Agayeva, S., AlMualla, M., et al. 2020, arXiv:2004.04277

Bellm, E. C., Kulkarni, S. R., Graham, M. J., et al. 2018, Publications of the Astronomical Society of the Pacific, 131, 018002

Bulla, M. 2019, Monthly Notices of the Royal Astronomical Society, 489, 5037–5045

Chambers, K. C., Magnier, E. A., Metcalfe, N., et al. 2016, arXiv e-prints, arXiv:1612.05560

Collaboration, T. L. S., the Virgo Collaboration, the KAGRA Collaboration, et al. 2013, arXiv:1304.0670

Cook, D. O., Kasliwal, M. M., Sistine, A. V., et al. 2019, The Astrophysical Journal, 880, 7

Coughlin, M. W., Tao, D., Chan, M. L., et al. 2018, Monthly Notices of the Royal Astronomical Society, 478, 692–702

Coughlin, M. W., Ahumada, T., Cenko, S. B., et al. 2019a, Publications of the Astronomical Society of the Pacific, 131, 048001

Coughlin, M. W., Dietrich, T., Antier, S., et al. 2019b, Mon. Not. Roy. Astron. Soc., 492, 863

Cowperthwaite, P. S., Berger, E., Villar, V. A., et al. 2017, The Astrophysical Journal, 848, L17

Feindt, U., Nordin, J., Rigault, M., et al. 2019, Journal of Cosmology and Astroparticle Physics, 2019, 005–005

Fong, W., Berger, E., Metzger, B. D., et al. 2013, The Astrophysical Journal, 780, 118

Goldstein, A., Veres, P., Burns, E., et al. 2017, The Astrophysical Journal, 848, L14

Gompertz, B., et al. 2020, arXiv:2004.00025

Graham, M. J., Kulkarni, S. R., Bellm, E. C., et al. 2019, Publications of the Astronomical Society of the Pacific, 131, 078001

Hotokezaka, K., Nakar, E., Gottlieb, O., et al. 2018, Nature Astronomy, arXiv:1806.10596

Kasen, D., Metzger, B., Barnes, J., Quataert, E., & Ramirez-Ruiz, E. 2017, Nature, 551, 80–84

Kasliwal, M. M., Kasen, D., Lau, R. M., et al. 2019, Monthly Notices of the Royal Astronomical Society: Letters, doi:10.1093/mnrasl/slz007

Kasliwal, M. M., Anand, S., Ahumada, T., et al. 2020, Kilonova Luminosity Function Constraints based on Zwicky Transient Facility Searches for 13 Neutron Star Mergers, arXiv:2006.11306

Kawaguchi, K., Kyutoku, K., Shibata, M., & Tanaka, M. 2016, The Astrophysical Journal, 825, 52

Kawaguchi, K., Shibata, M., & Tanaka, M. 2020, The Astrophysical Journal, 889, 171

Levan, A. 2020, PoS, Asterics2019, 044

Li, L.-X., & Paczyński, B. 1998, The Astrophysical Journal, 507, L59–L62

Lipunov, V. M., Gorbovskoy, E., Kornilov, V. G., et al. 2017, ApJ, 850, L1

Masci, F. J., Laher, R. R., Rusholme, B., et al. 2018, Publications of the Astronomical Society of the Pacific, 131, 018003

Metzger, B. D. 2019, Living Reviews in Relativity, 23, arXiv:1910.01617

Miller, C. 2017, Lectures on Gravitational Wave Astronomy

Mooley, K. P., Deller, A. T., Gottlieb, O., et al. 2018, Nature, 561, 355–359

Nakar, E. 2019, arXiv:1912.05659

Nousek, J. A., Kouveliotou, C., Grupe, D., et al. 2006, The Astrophysical Journal, 642, 389–400

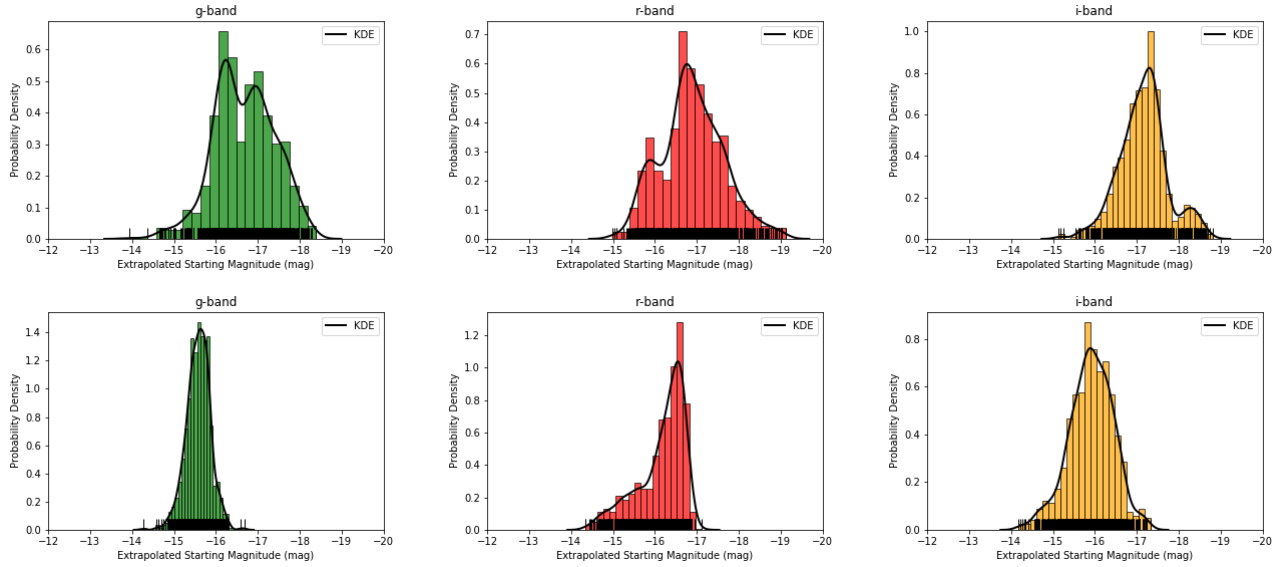Radice, D., Perego, A., Zappa, F., & Bernuzzi, S. 2018, The Astrophysical Journal, 852, L29

Fig. 14.— 1D histogram of peak magnitudes shown in g-, r-, and i-band left to right for BNS at the top. Similarly for NSBH at the bottom.
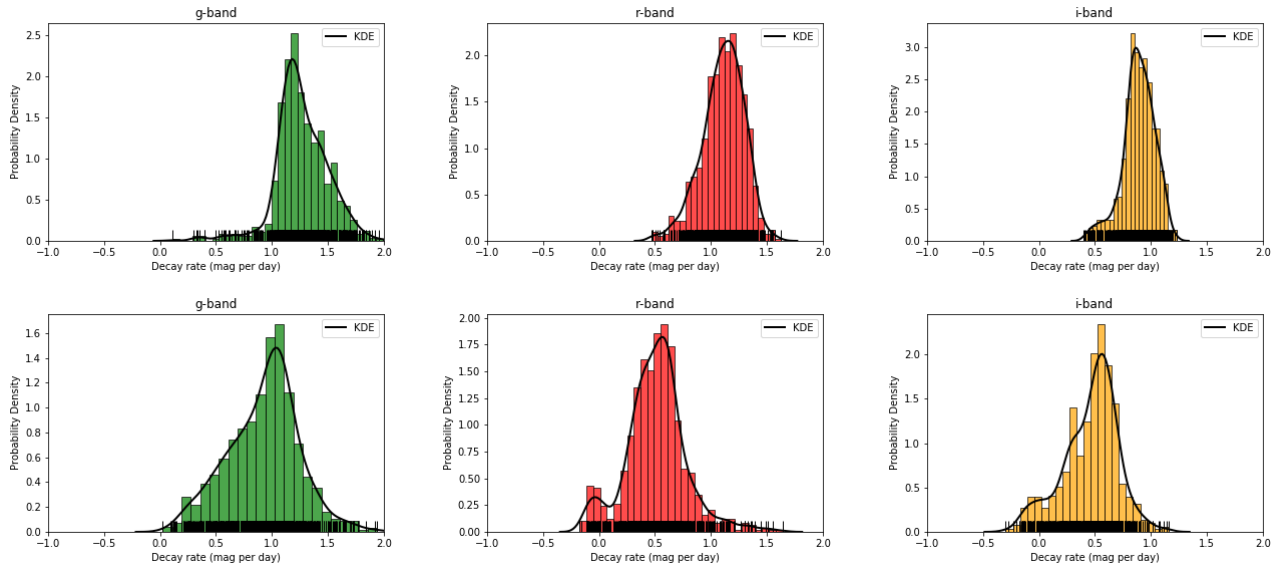

Fig. 15.— Top: BNS evolution rates from peak to 3 days later are shown in g-,r-, and i-band left to right. Similarly for NSBH in the bottom.

Riles, K. 2013, Progress in Particle and Nuclear Physics, 68, 1–54

Shappee, B. J., Prieto, J. L., Grupe, D., et al. 2014, The Astrophysical Journal, 788, 48

Soares-Santos, M., Holz, D.E., A.-J. C. R., & Herner, K. 2017, Astrophys. J. Lett., 848, L16

Tonry, J. L., Denneau, L., Heinze, A. N., et al. 2018, Publications of the Astronomical Society of the Pacific, 130, 064505

van Eerten, H. J., & MacFadyen, A. I. 2011, The Astrophysical Journal, 733, L37